Analysis and Control of PV Cascaded H-Bridge Multilevel Inverter With Failed Cells and Changing Meteorological Conditions

P. M. Lingom, *Student Member, IEEE*, Joseph Song-Manguelle, *Senior Member, IEEE*, Daniel Legrand Mon-Nzongo, *Member, IEEE*, Rodolfo César Costa Flesch, *Member, IEEE*, and Tao Jin, *Senior Member, IEEE*

***Abstract*—This article proposes an approach to control a photovoltaic cascaded H-bridge multilevel inverter with failed cells and changing meteorological conditions for large-scale grid-connected applications. The controller development is based on an analysis of the interaction between the inverter common-mode and differential-mode quantities, which is done in the time domain, supported by a space vector representation analysis. The proposed approach is able to produce balanced three-phase line-to-line voltages and currents even if there is a failed cell or if the fluctuating meteorological conditions cause uneven power distribution among the bridges. This is achieved through the modification of the pulsewidth modulation reference phase voltage angles combined to the injection of a dynamic homopolar component. Such an approach avoids tripping the system due to the protective functions #25 and #87 for per grid applicable codes and standards. Numerical simulations and laboratory experiments performed on a seven-level converter with different abnormal conditions to confirm the effectiveness of the suggested control strategy.**

***Index Terms*—Failure correction, inverters, photovoltaic (PV) cells, PV power systems, pulsewidth modulation (PWM).**

I. Introduction

With the continuous reduction of photovoltaic (PV) cell cost, large-scale grid-connected PV systems are getting a particular attention as a viable energy generation source [1]. There are several configurations of power conversion structures for PV systems, and a centralized configuration based on the cascaded H-bridge multilevel inverter (CHMI) topology is one of the most promising ones [2]. This happens mainly because of the modularity and flexibility associated with such configuration, given that it can be easily extended as needed with minimum modifications in its power part and in its modulation and control strategies [3]. Due to the high-voltage level required for high-power transmission, each H-bridge cell is fed by multiple isolated dc–dc converters to which PV arrays are connected [4]. Each dc–dc converter is controlled by an individual maximum power point tracking (MPPT) algorithm and a PV subconverter supplying a given H-bridge cell will produce a dc-link voltage $v_{\mathrm{dc},\,ij}$, where $i \in \boldsymbol{P} = \{a,\ b,\ c\}$; $j \in \boldsymbol{L} = \{1,\ 2,\ \ldots,\ k\}$ and k is the number of power modules per phase, as shown in Fig. 1.

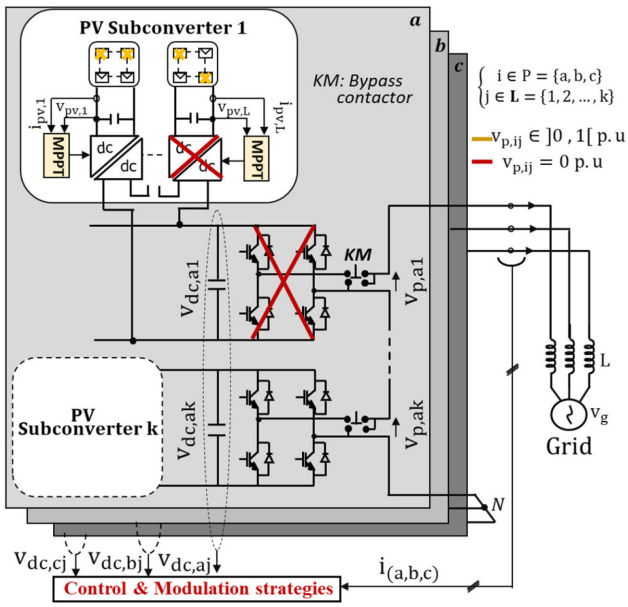

Fig. 1. Investigated system with failed PV cells and power modules.

In such configuration, each H-bridge power module is supplied by a set of PV cells that might produce unequal power distribution [5]. When partial shading occurs or any other meteorological condition changes, the output voltage of a given PV module changes, but the output voltage of the corresponding

Manuscript received March 6, 2020; revised May 16, 2020; accepted July 3, 2020. Date of publication July 14, 2020; date of current version September 22, 2020. This work was supported by the Chinese National Natural Science Foundation under Grants 51977039 and 51950410593. Recommended for publication by Associate Editor K. A. Kim. *(Corresponding author: Tao Jin.)*

P. M. Lingom and Tao Jin are with the Department of Electrical Engineering, Fuzhou University, Fuzhou 350116, China (e-mail: pascalm.lingom@fzu.edu.cn; jintly@fzu.edu.cn).

Joseph Song-Manguelle is with the Université du Québec à Trois-Rivières, Trois-Rivières, QC G8Z 4M3, Canada (e-mail: joseph.song@ieee.com).

Daniel Legrand Mon-Nzongo is with the Pearl Electric Co., Ltd., Guangzhou 511400, China (e-mail: monnzongo@fzu.edu.cn).

Rodolfo César Costa Flesch is with the Department of Automation and Systems, Federal University of Santa Catarina, Florianópolis 88040-900, Brazil (e-mail: rodolfo.flesch@ufsc.br).

Color versions of one or more of the figures in this article are available online at https://ieeexplore.ieee.org.

Digital Object Identifier 10.1109/TPEL.2020.3009107

dc/dc converter, which is fed by that PV module, can remain constant due to the MPPT control algorithm. However, in large-scale three-phase PV systems, each H-bridge is supplied by a set of isolated dc/dc converters and the total output voltage of these individual dc/dc converters forms the individual dc-link voltage of a given H-bridge ($v_{\mathrm{dc},\,ij}$) [6]. It has been assumed for sake of simplicity in this analysis that MPPTs of a given H-bridge are independent and are not supervised by a local H-bridge controller that could have kept their respective output voltages equal, regardless of the meteorological conditions or shading of panels. Also, there is no phase-level master controller that can keep the dc-link voltage produced by the set of dc/dc converters for all series connected H-bridges in that phase to remain equal. Moreover, for a given H-bridge power cell, the PV modules supplying dc–dc converters and the dc/dc converter on that specific H-bridge cell can fail, leading to a total dc-link voltage different to its nominal value [7]. Therefore, with such system configuration, a PV voltage mismatch can result from changing meteorological conditions, a failure of PV modules or a failure of dc/dc converters producing the dc-link voltage of a given H-bridge [8]. In ideal conditions, $v_{\mathrm{dc},\,ij} = 1$ p.u., $\forall i \in \boldsymbol{P}$, $j \in \boldsymbol{L}$. When a PV voltage mismatch occurs, $v_{\mathrm{dc},\,ij} \in]0\ ,\ 1[$ p.u. leading a distribution of different dc-voltage values at the input dc links of H-bridges.

Such dc-link voltage inequality between different H-bridge cells on the same inverter phase produces interbridge power imbalance, which then leads to a power imbalance between the three phases called interphase power imbalance [9]. Both power imbalances can affect the control and proper operation of the CHMI by injecting unbalanced voltages and currents to the grid, which is not tolerated by the grid application codes and standards [10].

The effect is similar when the system operates with one or more failed H-bridge power modules. A power module includes the hardware of power electronic converters, as well as the associated control board. When the failure of any of these components occurs, the gating signals to that specific H-bridge power module are blocked and its output is bypassed, leading to unbalanced inverter output voltages and currents and a reduction of the overall system productivity [11].

To solve power imbalanced issues in such a system, two types of control methods have been already proposed in the literature, namely, the feedforward control method and the zero-sequence injection method. The feedforward control method has been developed to solve the interbridge power imbalance issue [8], [11], whereas zero-sequence injection methods have been proposed to solve the interphase power imbalance issue [9]–[12]. The optimal zero-sequence injection method is considered as one of the most advanced control strategies developed to solve the imbalance power issue in the grid-connected PV inverter applications [12]. This method is able to provide balanced inverter output currents even with severe uneven power distribution among the bridges. Unfortunately, such an approach has been limited for this purpose regardless of the fact that the inverter phase voltages can be unbalanced due to the failed cells or fluctuating environmental conditions, such as unequal received irradiance levels, different ambient temperature, aging and/or inconsistence degradation of the PV panels. In industrial application, if under aforementioned operating conditions the inverter produces an output voltage with magnitudes that are significantly smaller than the ones required to be connected to the grid, a generator synchronizing check protective function #25 of the protective relay will close the output breaker and block that inverter from connecting to unsynchronized grid voltage. A balanced three-phase current is required to avoid tripping the differential protective function #87 of protective relays, whereas a balanced three-phase voltage is required to enable synchronization between the inverter and the grid voltages permissive from protective function # 25 [13].

To produce both balanced inverter output line-to-line (LL) voltages and currents under fluctuating environmental conditions and, at the same time, be able to deal with failed power modules, this article proposes a generalized neutral-shift strategy through the modification of phase voltage angles combined to a min–max zero-sequence component injection. The objective of the neutral-shift strategy through the modification of inverter phase voltage angles is to rebalance the LL voltages regardless of the fact that the line-to-neutral (LN) voltages may be imbalanced. This strategy was initially developed by Hammond [14] and its application remains limited to variable speed drives, where any damaged and bypassed H-bridge cell sets the corresponding dc-link voltage to zero ($v_{\mathrm{dc},\,ij} = 0$) [14]–[16], [20], [23], [24]. In this article, the method is extended and generalized for a large-scale PV grid-connected application, taking into account fractional dc source voltages ($v_{\mathrm{dc},\,ij} \in]0\ ,\ 1[$ p.u.) with respect to their nominal values, which is a quite normal phenomenon caused by changing meteorological conditions. An average min–max homopolar component is utilized to extend the converter operating range while maintaining each phase within its linear operation range even if there is a failed cell or if the meteorological conditions cause uneven power distribution among cells.

The overall controller development is based on an analysis of the interaction between the inverter common-mode and differential-mode quantities, which is done in the time domain, supported by a space vector representation. The dependence of the common-mode quantities with respect to the differential-mode quantities in normal (ideal), abnormal, and corrected operation modes is presented. This analysis is needed to determine the linear region boundaries of all possible common-mode/homopolar components to be injected during the compensation mechanism for a given abnormal condition.

The proposed modulation and control strategies are implemented in the voltage-oriented control structure, where both *dq*-currents are regulated by a multivariable proportional-integral (PI) controller. The compensation mechanism through the readjustment of phase voltage angles is introduced into the $dq-abc$ transformation stage, whereas the average min–max homopolar component is injected in a phase-disposition (PD) pulsewidth modulation (PWM) process. Such a control approach has a wide applicability in both grid-tie and standalone applications. Moreover, it allows a better utilization of PV sources connected to the grid and, at the same time, increases the robustness of the solution to failed converter modules.

II. System Behavior in Normal Operation Mode

A. Theoretical Considerations

The developments of this article consider k series-connected H-bridge power modules in each phase of a three-phase system. Each H-bridge module is supplied by an isolated dc voltage $v_{\mathrm{dc},\,ij}$, such that $0 \leq v_{\mathrm{dc},\,ij} \leq 1$, where $i \in \boldsymbol{P}$ and $j \in \boldsymbol{L}$.

In an ideal operating condition, $v_{\mathrm{dc},\,ij} = 1$ p.u. and the output voltage of each H-bridge is written as $v_{p,\,ij} \in \boldsymbol{K} = \{-v_{\mathrm{dc},\,ij},\ 0,\ v_{\mathrm{dc},\,ij}\}$. The three-phase PWM reference voltage is $v^*_{r,i}(t)$, whereas $v_i(t)$ is the inverter LN voltage. The neutral point corresponds to any common reference point of the system, even if it cannot be directly accessed. The inverter output voltage is given by

$$v_i\,(t) = \sum_{j=1}^{k} v_{p,ij}\,(t)\,. \tag{1}$$

For the PWM modulator to remain within its linear modulation range, the following criteria should be met for each phase [17]:

$$|v_i\,(t)| \leq \sum_{j=1}^{k} v_{\mathrm{dc},ij} = V_{\mathrm{dc},\,i}. \tag{2}$$

In ideal condition, the PWM method with sinusoidal reference $v^*_{r,i}(t)$ at a fundamental frequency ω_0 and a modulation index m is given by

$$v^*_{r,i}\,(t) = mV_{\mathrm{dc},\,i}\sin\left(\omega_0 t - (i-1)\,\frac{2\pi}{3}\right). \tag{3}$$

And the achievable converter leg voltage is defined such that

$$\max_{i\,\in\,\boldsymbol{P}} v_i\,(t) = v_i(x^*\,) = V_{\mathrm{max},i}\ \ \forall x^* \in \operatorname*{argmax}_{i\,\in\,\boldsymbol{P}} v_i\,(t) \tag{4a}$$

$$V_{\mathrm{max},i} = \frac{\sqrt{3}}{2} V_{\mathrm{dc},\,i}. \tag{4b}$$

Understanding the behavior of differential- and common-mode quantities produced by the PV cascaded H-bridge (CHB) inverter in ideal conditions is important for analyzing the behavior of such converter under abnormal operating conditions such as fluctuating environmental conditions or failed cells

B. Time-Domain Analysis of System in Normal Mode

As described in [18], the common-mode voltage corresponds to any voltage quantity common to all the three phases, whereas the common-mode current is any current quantity returning to the grid through any common path other than the three phases; such path includes an intentional ground impedance or a leakage impedance, as well as intentional neutral wire. As the system being analyzed is a voltage source system, the analysis will be focused on the voltages only. Even if common-mode quantities do not produce any power, they can affect how the power is produced by the converter [19]. For the three-phase PWM inverters, a common-mode voltage can be added to the LN reference voltages usually given in *abc*-reference frame, to modify the differential-mode voltages. A modified PWM reference $v^*_i(t)$ with a common-mode component $v_0(t)$ injection can be expressed as follows:

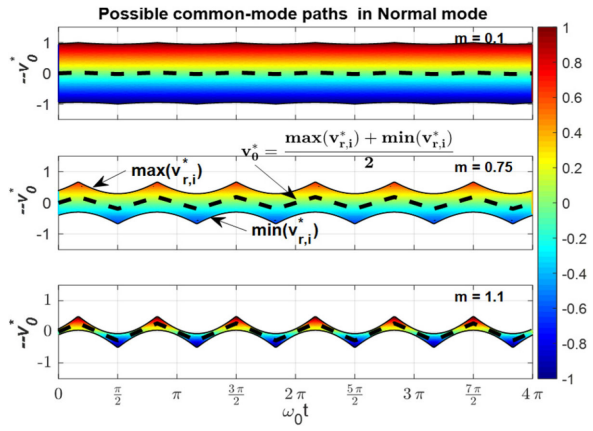

Fig. 2. Homopolar component ranges for different modulation indices in normal operation mode.

$$v^*_i\,(t) = v^*_{r,i}\,(t) + v^*_0\,(t)\,. \tag{5}$$

It is usually convenient to choose a homopolar component, which is the average value within its permitted limits [17], such that

$$v_0\,(t) = \frac{\min\limits_{i\,\in\,\boldsymbol{P}} v^*_{r,i}\,(t) + \max\limits_{i\,\in\,\boldsymbol{P}} v^*_{r,i}\,(t)}{2}. \tag{6}$$

Theoretically, the homopolar component can assume values that satisfy $-1 \leq v_0(t) \leq 1$ (in per unit of the phase voltage) to maintain the modulator in the linear region, depending on the modulation index. This result can be illustrated by a simple geometric analysis of the 2-D surfaces shown in Fig. 2, where the min–max homopolar component is highlighted. In this figure, we can observe that the smaller the modulation index, the larger its variation boundaries. It can be also seen that the possibilities to select the common-mode component are reduced by increasing the modulation index, which represents the differential-mode in this case. Fig. 3 shows the modified PWM reference voltages with the injection of the min–max homopolar component, as well as the time-domain output voltages generated by the multilevel inverter (with $k = 3$ H-bridges per phase) for a modulation index of 1.1. In ideal operation, the injection of the min–max homopolar component into the converter reference voltage allows to extend the modulation index (differential mode voltage) above 1 without being into the overmodulation region. This degree of freedom can be restricted in abnormal conditions, i.e., when the converter is operating under fluctuating meteorological conditions or with failed cells [17].

C. Space Vector Analysis of System in Normal Mode

As described in [20], the three-phase inverter LN voltages $v_i,\ \ i \in \boldsymbol{P}$, can be transformed into $v_{\alpha\beta 0}$ as follows:

$$v_i = [v_a\ v_b\ v_c]^T;\ v_{\alpha\beta 0} = [v_\alpha\ v_\beta\ v_0]^T \tag{7a}$$

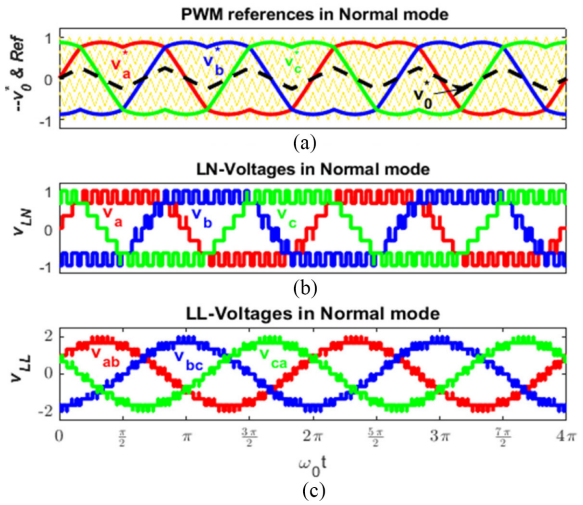

Fig. 3. Time-domain representation of a system behavior in normal operation mode, $f_c/f_0 = 25; m = 1.1$.

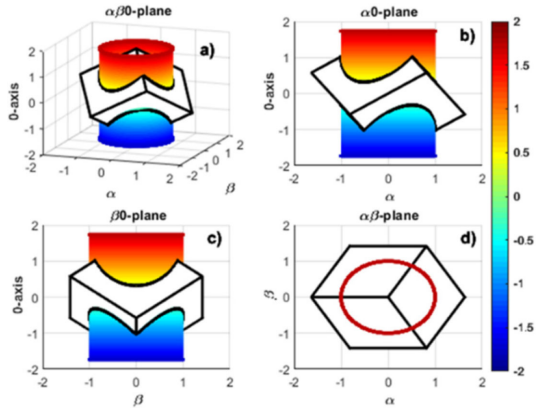

Fig. 4. Space vector representation of the differential-mode and common-mode in normal operation mode (theoretical limits of the homopolar component).

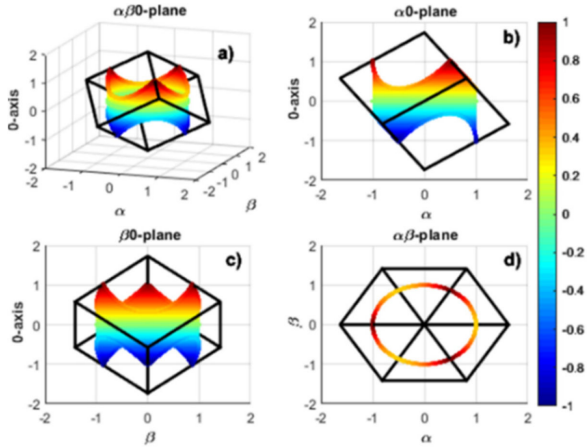

Fig. 5. Space vector representation of the differential-mode and common-mode in normal operation mode (practical limits of the homopolar component).

$$v_{\alpha\beta 0} = M v_i \tag{7b}$$

$$M = \sqrt{\frac{2}{3}} \begin{bmatrix} 1 & -1/2 & -1/2 \\ 0 & \sqrt{3}/2 & -\sqrt{3}/2 \\ 1/\sqrt{2} & 1/\sqrt{2} & 1/\sqrt{2} \end{bmatrix}. \tag{7c}$$

Based on (7a), the differential-mode quantities are v_α and v_β, whereas the common-mode quantity is the homopolar component v_0. In normal (ideal) conditions, there is a total of 3^kswitching states that the inverter can generate, which form a regular cube in the 3-D $\alpha\beta 0$ plane and the borders of this cube correspond to the largest voltages that the converter can generate on each phase [21], [22]. However, in abnormal conditions all the possible voltage states cannot be generated (as shown in Section III). As mentioned in Section II-B, a common-mode voltage component can be added to the PWM LN reference voltages to modify the inverter differential-mode voltages. Therefore, the influence of the possible common-mode voltage on the inverter differential-mode quantities can be analyzed through the space vector representation of the PWM reference vector with respect to the inverter states [21], [22]. In fact, the application of the transformation in (7b) to the original reference vector $v^*_{r,i}$ provides a vector $v^*_{r,\alpha\beta 0}$, which describes a circle in the $\alpha\beta$ plane, as shown in Fig. 4(d). Since the common-mode voltage quantity moves along the 0-axis, a cylinder parallel to this axis is obtained for all theoretical possible common-mode quantities, as illustrated in Fig. 4(a). The interactions between each differential-mode quantity and the reference-voltage cylinder are isolated in Fig. 4(b) and (c). As it is clearly seen, common-mode voltage components vary within a boundary $-\sqrt{3} \le h \le \sqrt{3}$, where h represents the height of the theoretical cylinder.

To ensure the PWM modulator remains within its linear region in ideal condition, all possible common-mode components to be injected should not exceed the differential-mode limits [21]–[23]. Because of that, only the part of the cylinder that is contained in the inverter output-voltage cube shall be considered, as illustrated in Fig. 5(a). The dependence of the common-mode quantity with respect to the differential-mode into the $\alpha 0$ and $\beta 0$ planes is shown in Fig. 5(b) and (c), respectively. The borders of the intersected cylinder surface correspond to the minimum $(h_{\min})$ and maximum$(h_{\max})$ achievable common-mode voltage component that can be injected to the phase voltages in order to keep the PWM modulator within its linear region [21], [22]. A total achievable height of this intersected cylinder surface can be determined as follows:

$$h' = h_{\max} - h_{\min} \tag{8a}$$

$$h' = 2\sqrt{3} - \sqrt{2}\left(\max v^*_{r,i}(t) - \min v^*_{r,i}(t)\right) \tag{8b}$$

with

$$h_{\max} = \sqrt{3} - \sqrt{2}\max v^*_{r,i}(t) \text{ and}$$

$$h_{\min} = -\sqrt{3} + \sqrt{2}\min v^*_{r,i}(t).$$

These limits must be respected in the design of the PWM strategy under a dc voltage inequality between power modules

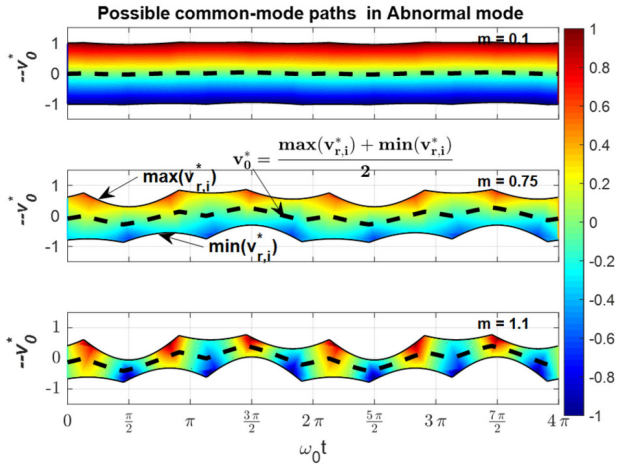

Fig. 6. Homopolar component ranges for different modulation indices in abnormal operation mode: $v_{\mathrm{dc},\,a} = [1\ 1\ 1]$; $v_{\mathrm{dc},\,b} = [0\ 0.2\ 1]$; $v_{\mathrm{dc},\,c} = [0.7\ 1\ 0.3]$.

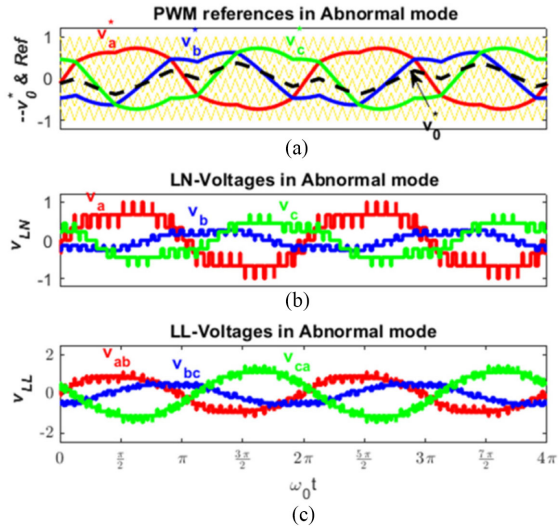

Fig. 7. Time-domain representation of a system behavior in abnormal operation mode, $f_c/f_0 = 25$; $m = 1.1$: $v_{\mathrm{dc},\,a} = [1\ 1\ 1]$; $v_{\mathrm{dc},\,b} = [0\ 0.2\ 1]$; $v_{\mathrm{dc},\,c} = [0.7\ 1\ 0.3]$.

on the same phase resulting from changing meteorological conditions, a failure of PV modules, or a failure of dc/dc converters as developed in the next.

III. System Behavior in Abnormal Operation Mode

A. Time-Domain Analysis of the System in Abnormal Mode

In ideal operating conditions, each PV subconverter is designed to generate a nominal dc-link voltage $v_{\mathrm{dcnom},\,ij} = 1$ p.u .and the output voltage of each H-bridge is given such that $v_{\mathrm{pnom},\,ij} \in \{-1,\ 0,\ 1\}$p.u. Abnormal condition occurs when this is not met due to the failed cells or fluctuating environmental conditions. When a PV voltage mismatch occurs, $v_{\mathrm{dc},\,ij} \in]0\ ,\ 1[$ p.u., and when there is a failure of H-bridge power module, $v_{\mathrm{dc},\,ij} = 0$ and $v_{p,\,ij} = 0$.

If any of aforementioned abnormal operating conditions is not taken into consideration in the control system or modulation, the total dc voltage available for all H-bridges on that phase will decrease, leading to unbalanced inverter output voltages and currents, which is not tolerated by the grid application codes and standards [13]. Fig. 6 shows the homopolar boundaries for a given abnormal condition defined for $k = 3$ H-bridges per phase and voltage vectors given by: $v_{\mathrm{dc},\,a} = [1\ \ 1\ 1]$; $v_{\mathrm{dc},\,b} = [0\ 0.2\ 1]$; and $v_{\mathrm{dc},\,c} = [0.7\ \ 1\ \ 0.3]$. In this considered abnormal condition, phase *b* contains a failed power module and a partial dc-link voltage supply for the second H-bridge, whereas phase *c* contains two H-bridges with partial dc-link voltage supply. As illustrated in this figure, despite the severity of the considered abnormal condition, the common-mode band provides enough flexibility to adjust the differential mode in order to improve the converter behavior. Under unequal power distribution among the bridges, the converter reference voltages can be modified through the injection of an appropriate common-mode voltage component in order to influence the current flowing into each phase. However, the injection of zero-sequence component method does not produce balanced inverter output voltages, as shown in Fig. 7(b) and (c), where the corresponding converter LN and LL voltages are unbalanced, respectively.

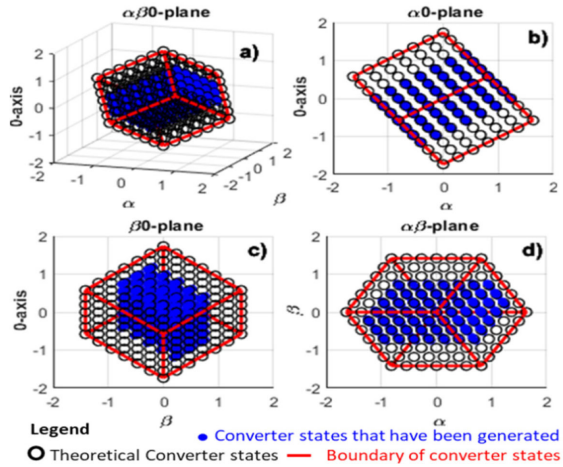

Fig. 8. Space vectors of the inverter voltage states in abnormal mode: $v_{\mathrm{dc},\,a} = [1\ 1\ 1]$; $v_{\mathrm{dc},\,b} = [0\ 0.2\ 1]$; $v_{\mathrm{dc},\,c} = [0.7\ 1\ 0.3]$.

B. Space Vector Analysis of the System in Abnormal Mode

The discussed abnormal condition remains the same as the one used in Section III-A. All possible inverter voltage states and their interpolated limits are shown in Fig. 8, as well as the theoretical boundaries of the differential-mode quantity. As illustrated in this figure, the converter cannot generate all its theoretical voltage states due to the severity of the abnormality (a drastic degradation of the meteorological conditions in phases *b* and *c*, and a failed power module in phase *c*). Fig. 9 shows the boundaries of all achievable common-mode voltage solutions inscribed within the differential-mode quantity boundaries. The dotted lines are the limits of the system in normal operation, whereas the solid lines are the limits of the system in abnormal

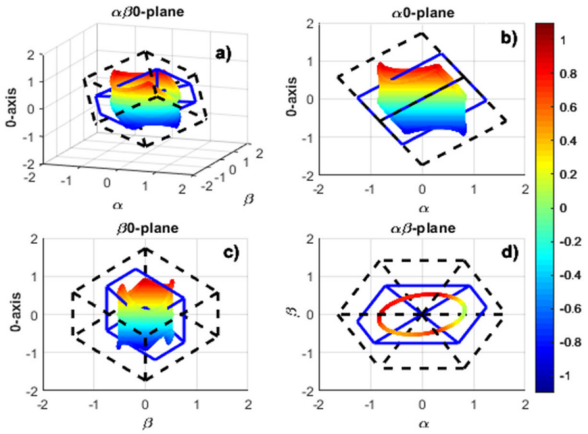

Fig. 9. Space vector representation of the differential-mode and common-mode in abnormal operation mode (practical limits of homopolar component): $v_{\mathrm{dc},\,a} = [1\ 1\ 1]$; $v_{\mathrm{dc},\,b} = [0\ 0.2\ 1]$; $v_{\mathrm{dc},\,c} = [0.7\ 1\ 0.3]$.

operation mode. In Fig. 9(a), we can observe that some segments of the inverter output-voltage cube have become smaller than their original values, so the linear modulation band has changed, as well as the fluctuation range of the homopolar component. In addition, the elliptical path described by the unbalanced reference voltages in $\alpha\beta$ plane [see Fig. 9(d)] demonstrates that the converter will produce unbalanced LL voltages if the reference voltages are not adjusted accordingly.

To rebalance the inverter LL voltages under uneven power distribution among the bridges, the neutral-shift strategy through the modification of the phase voltage angles can be applied [7]. This can be achieved by finding the equilateral triangle in a circle inscribed inside the irregular hexagon. The boundaries of that irregular hexagon correspond to the maximum feasible limits of the PV inverter differential-mode voltage under fluctuating meteorological conditions or failed cells.

IV. System Behavior in Corrected Operation Mode

A. Neutral-Shift Strategy

In this article, the neutral-shift strategy through the modification of phase voltage angles is extended and generalized for a large-scale grid-connected PV application, taking into account fractional dc source voltages ($v_{\mathrm{dc},\,ij} \in]0\ ,\ 1[$ p.u.), which are not considered in the original formulation. The idea is to move the converter neutral point to a new position by adjusting its phase voltage angles when the converter phase voltages are operating with different amplitudes due to the fluctuating environmental conditions. This results to a "perceived" balanced output LL voltages, regardless of the fact that the phase-to-neutral voltages may be imbalanced. In addition, the method is still able to deal with failed H-bridges modules ($v_{\mathrm{dc},\,ij} = 0$).

Fig. 10 illustrates the general diagram for the angles calculation. The equilateral triangle means the relationship between LN voltages (black solid lines) and LL voltages (red solid lines) for a given operating condition. The problem to be solved is to find the corresponding phase voltage angles required to generate balanced LL voltages when the LN voltages of the

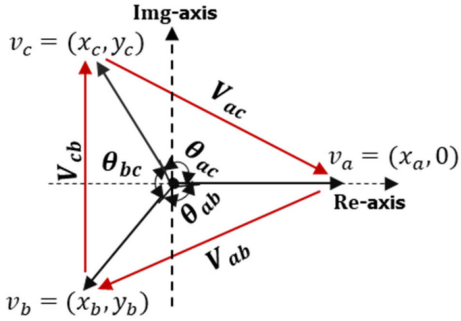

Fig. 10. General diagram for angles calculation.

inverter have different amplitudes due to abnormal operating conditions. Based on this diagram, the mathematical solution is found by solving (9), as initially described in [24]. After some mathematical manipulations, the result leads to a system of four nonlinear equations with four unknowns, x_b, y_b, x_c, and y_c, as defined in (10)

$$|\overrightarrow{v_{ba}}| = |\overrightarrow{v_{ac}}| = |\overrightarrow{v_{bc}}| \tag{9}$$

$$\begin{cases} (x_b - x_c)^2 + y_b{}^2 = (x_c - x_a)^2 + y_c{}^2 \\ (x_b - x_c)^2 + y_b{}^2 = (x_c - x_b)^2 + (y_c - y_b)^2 \\ v_b{}^2 = x_b{}^2 + y_b{}^2 \\ v_c{}^2 = x_c{}^2 + y_c{}^2. \end{cases} \tag{10}$$

Theoretically, the phase voltage angles are obtained from

$$\begin{cases} \theta_{ab} = \arctan\left(\frac{y_b}{x_b}\right) \\ \theta_{ac} = \arctan\left(\frac{y_c}{x_c}\right) \\ \theta_{bc} = 2\pi - (\theta_{ab} + \theta_{ac})\,. \end{cases} \tag{11}$$

As discussed in [16], for a given abnormal condition, each solution x_b, y_b, x_c, and y_c of the system of equations (10) has multiple values, and not all of the angle values obtained from (11), which can be used to provide the maximum achievable balanced LL voltage. For instance, in the case of the considered abnormal condition, the values of the angles obtained from (11) are given such as: $\theta_{ab} \in \{33, 23^\circ,\ 86.5^\circ\}$ and $\theta_{ac} \in \{44, 11^\circ,\ 75.5^\circ\}$. This implies that the maximum balanced LL voltage that can be reached in this case can only be generated with $\theta_{ab} = 86.5^\circ$ and $\theta_{ab} = 75.5^\circ$. To achieve a systematic selection of the phase voltage angles during the compensation mechanism with the capability to provide the maximum achievable balanced output LL voltage under abnormal operating conditions, this article proposes an appropriate solution defined as follows:

$$\begin{cases} \theta_{ab} = \max\left[\arctan\left(\frac{y_b}{x_b}\right)\right] \\ \theta_{ac} = \max\left[\arctan\left(\frac{y_c}{x_c}\right)\right] \\ \theta_{bc} = 2\pi - (\theta_{ab} + \theta_{ac})\,. \end{cases} \tag{12}$$

Fig. 11 represents the phasor diagrams of LN and LL voltages of the converter in normal, abnormal, and corrected operation modes. In normal operation mode, as shown in Fig 11(a), both LN and LL voltages are balanced and the phase angles between *a* and *b/c* is 120°, i.e., $\theta_{ab} = -120^\circ$, $\theta_{ac} = 120^\circ$, and

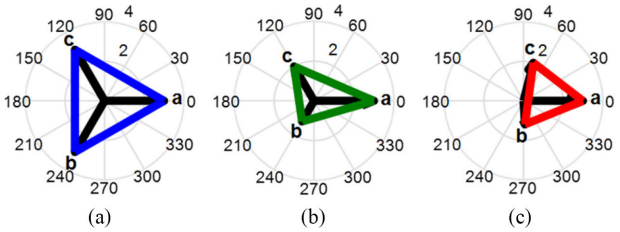

Fig. 11. Voltage phasor diagram for different operation modes. (a) Normal operation. (b) Abnormal operation. (c) Corrected operation.

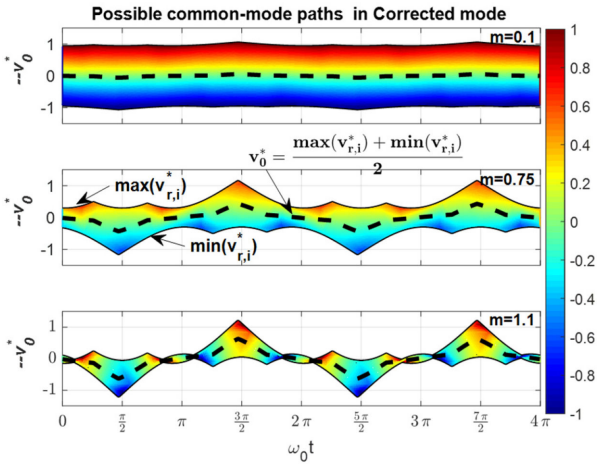

Fig. 12. Homopolar component ranges for different modulation indices in corrected operation mode.

$\theta_{bc} = 120°$. In abnormal mode, as shown in Fig 11(b), both LN and LL voltages are unbalanced and the phase angles remain 120°. The considered abnormal condition is: $v_{\mathrm{dc},\,a} = [1\ \ 1\ 1]$; $v_{\mathrm{dc},\,b} = [0\ 0.2\ 1]$; and $v_{\mathrm{dc},\,c} = [0.7\ 1\ \ 0.3]$. To correct this system, the magnitudes of LL voltages have to be adjusted and settled at a value where they are all equal, as shown in (9), then the corresponding angles have to be computed to fulfill this condition, as expressed in (10). As shown in Fig 11(c), the phase voltage angles have been adjusted and phase *a* is displaced from phase *b* by 86.5° and from phase *c* by 75.5°.

B. Time-Domain Analysis of the Corrected System

Fig. 12 shows the achievable limits of all possible common-mode voltages to be injected for different modulation indices after applying the neutral-shift strategy for the considered abnormal condition. By selecting any homopolar component within these bands, balanced LL voltages are maintained and balanced currents are produced for the discussed abnormal condition. The compensated PWM references and the corresponding LN and LL converter voltages obtained based on the modification of the phase voltage angles combined with the injection of the min–max homopolar component are shown in Fig. 13. In this figure, it can be observed that the LL voltages are successfully rebalanced, whereas the LN voltages are not unbalanced. Since the neutral-shift method has nothing to do with keeping the

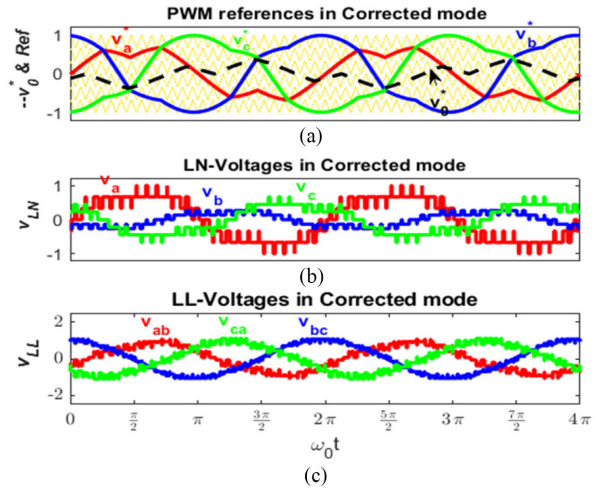

Fig. 13. Time-domain representation of a system behavior in corrected operation mode, $f_c/f_0 = \ 25; m = 1.1$.

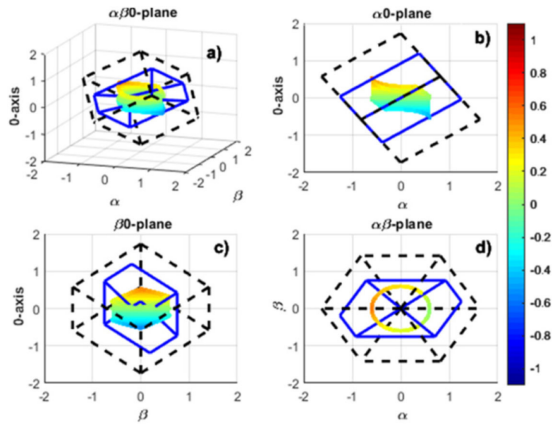

Fig. 14. Space vector representation of the differential mode and common mode in corrected mode (practical limits of homopolar).

PWM modulator in its linear region, a min–max homopolar component is injected to avoid overmodulation or saturation.

C. Space Vector Analysis of the Corrected System

Fig. 14 shows the boundaries of the differential-mode voltages, as well as the new limits for the homopolar component obtained by applying the neutral-shift strategy to compensate the considered abnormal condition. This is performed by transforming the set of unbalanced three-phase reference voltages to the stationary $\alpha\beta$ plane according to the modified phase angles. In fact, when the neutral-shift strategy is applied under abnormal conditions, the phase angles between *a* and *b* or *c* are no longer 120° and the *abc* to $\alpha\beta$ transformation matrix *M* given in Section II-C can be modified by considering the actual angles, as follows:

$$M' = \sqrt{\frac{2}{3}} \begin{bmatrix} 1 & \cos(\theta_{ab}) & \cos(\theta_{ac}) \\ 0 & \sin(\theta_{ab}) & \sin(\theta_{ac}) \\ 1/\sqrt{2} & 1/\sqrt{2} & 1/\sqrt{2} \end{bmatrix}. \qquad (13)$$

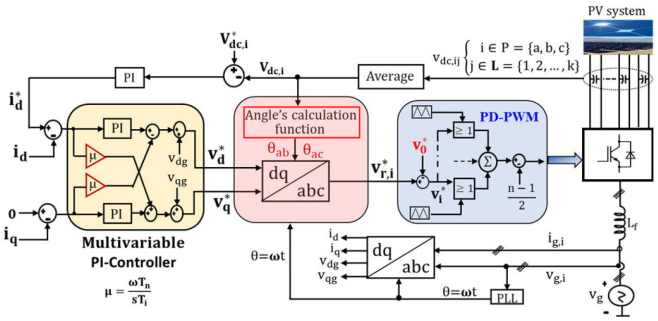

Fig. 15. Proposed overall control structure.

The impact of the modified abc to $\alpha\beta$ transformation matrix (13) is shown in Fig. 14(d), where the unbalanced PWM references describe a circle in the $\alpha\beta$ plane. This results in a perceived balanced LL voltage.

V. Summary of the Proposed Control and Modulation Strategies

The aim of this section is to present the proposed overall control structure and describe how the compensation mechanism can be carried out online by tolerating the different abnormal operating conditions. The proposed overall control architecture is shown in Fig. 15. In this structure, the outer loop performs the control of the total dc source voltages, which determine the overall active power P (proportional to i_d^*) to be injected to the grid [25]. The reactive current reference i_q^* is set to zero for a unity power factor operation. The inner current loop control is based on a multivariable-PI controller with antiwindup. This controller is chosen because it offers a greater robustness compared to the conventional inductor current state feedback approach [26]. This feature is an important aspect to consider when the system operates in closed loop under severe fault conditions, since it can provide the dq-PWM references with negligible overshoot and low distortion and ripples, which will ease the compensation mechanism.

To reduce the computation time during the compensation mechanism, the symbolic equation (10) has been solved offline, and only its parameterized results are implemented in the controller and executed whenever there is a dc-link voltage fluctuation in any phase within two consecutive sampling instants. It has to be noted that there is a significant difference between a fluctuating dc-link voltage and a failed power cell. The fluctuation of the dc-link voltage is corrected through online angle readjustment, whereas a failed power cell requires the following tasks to be executed: fault detection; deactivation of all PWM pulse signals; initiation of failed power module physical isolation and bypass mechanisms; calculation of angle alteration according to (12); detection of grid voltage and synchronization of the reference on-the-fly; reactivation of all PWM pulse signals. This transient period can realistically last up to 250 ms, where no power is produced. Usually, as mentioned in [27], the neutral-shift method applied to variable-frequency drive (VFD) lasts about 500 ms in large industrial applications. The angle calculation function is introduced into dq-abc transformation stage to update the coefficients of the inverse Park matrix whenever there is a dc-link voltage fluctuation in any inverter phase. The compensated PWM reference voltages are then obtained through the modified $dq-abc$ transformation given as follows:

$$\begin{bmatrix} v_a^* \\ v_b^* \\ v_c^* \end{bmatrix} = \begin{bmatrix} 1 & 0 \\ \cos(\theta_{ab}) & \sin(\theta_{ac}) \\ \cos(\theta_{ac}) & \sin(\theta_{ab}) \end{bmatrix} \begin{bmatrix} \cos(\theta) & -\sin(\theta) \\ \sin(\theta) & \cos(\theta) \end{bmatrix} \begin{bmatrix} v_d^* \\ v_q^* \end{bmatrix}. \tag{14}$$

The average min–max homopolar component is utilized to prevent the converter for entering in the overmodulation area. Under a given abnormal condition, this component become dynamic, since it readjusts itself based on the reference voltages provided from the modified $dq-abc$ transformation block. Finally, the PD PWM strategy is used because it provides a better output voltage quality with superior harmonic performance [18].

VI. Numerical Validations

The proposed control and modulation strategies have been implemented in a hardware-in-the-loop real-time system. It uses host-target structure with the host PC running MATLAB/Simulink and target PC running a real-time kernel. The power stage, including the PV cells, the power electronics, and the grid are developed in a Simulink environment. During the cosimulation, the host PC compiles and loads the DSP code (Simulink bloc diagrams) to the target PC via a transmission control protocol/internet protocol (TCP/IP) communication.

For large-scale PV system, the investigated system can be scaled for several megawatts. Therefore, the converter produces medium-voltage to reduce the insulated-gate bipolar transistor (IGBT) current rating. In this section, it has been assumed that the converter is connected to grid at the 3.3 kV substation bus. However, depending on the overall power to be collected, such a converter can reach 11 kV [27].

A. Simulations in Steady State

Two illustrative abnormal cases are discussed as follows.

Case #1: $v_{dc,a} = [0.5\ 0\ 0.5]$; $v_{dc,\,b} = [\,1\ 1\ 1\,]$; and $v_{dc,\,c} = [1\ 1\ \ 1\,]$. In this case, the inverter phase a is operating with a failed power module ($a1$) and a partial dc-link voltage supply for modules $a2$ and $a3$ due to the PV panel mismatches. There is no abnormal condition in phases b and c. This abnormal condition causes unbalanced voltages and currents into the grid, as shown in Fig. 16(a). However, when the proposed control method is applied, the three-phase LL voltages and currents are successful rebalanced, as shown in Fig. 16(b). This is achieved with $\theta_{ab} = -140.4°$ and $\theta_{ac} = 140.4°$.

Case #2: $v_{dc,a} = [1\ 1\ 1]$; $v_{dc,\,b} = [\,0.3\ 1\ 0.7\,]$; and $v_{dc,\,c} = [1\ 0.6\ \ 0.4\,]$. In this case, the inverter phases b and c contain two H-bridge cells with partial dc-link voltage supply caused by the fluctuating environmental conditions in their respective PV panels. As shown in Fig. 17(a), both (LN and LL) voltages and currents are unbalanced because the inverter is operating without any correction method. However, LL voltages and currents are successfully rebalanced with the proposed approach, as shown in Fig. 17(b), which confirms

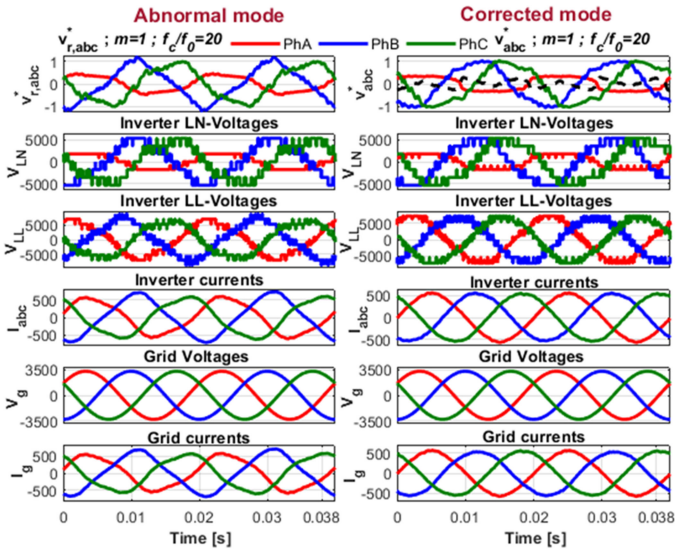

Fig. 16. Simulation results for a seven-level CHB inverter with $f_c/f_0 = 20$: $v_{\mathrm{dc},\,a} = [0.5\ \ 0\ \ 0.5]$; $v_{\mathrm{dc},\,b} = [1\ \ 1\ \ 1]$; $v_{\mathrm{dc},\,c} = [1\ \ 1\ \ 1]$, $m = 1$.

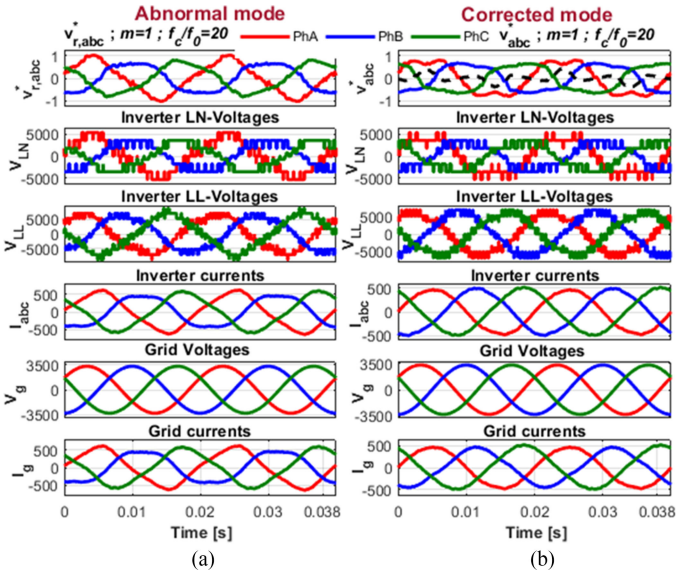

Fig. 17. Simulation results for a seven-level CHB inverter with $f_c/f_0 = 20$: $v_{\mathrm{dc},\,a} = [1\ \ 1\ \ 1]$; $v_{\mathrm{dc},\,b} = [0.3\ \ 1\ \ 0.7]$; $v_{\mathrm{dc},\,c} = [1\ \ 0.6\ \ 0.4]$, $m = 1$.

the effectiveness of the proposed strategy. The modified phase voltage angles are: $\theta_{ab} = -101.4^\circ$ and $\theta_{ac} = 101.4^\circ$.

B. Simulations With Transients

Two cases have been simulated. In *Case A*, partial dc-link voltages are suddenly changed while the system is running in normal operating mode. In *Case B*, a sudden loss of one power module occurs.

Case A: The initial operating condition is $v_{\mathrm{dc},\,a} = [1\ 1\ 1]$; $v_{\mathrm{dc},\,b} = [1\ 1\ 1]$; $v_{\mathrm{dc},\,c} = [1\ 1\ 1]$, i.e., the system is in normal operating mode. Then, at $t = 0.03$ s, sudden step changes are simultaneously applied to dc-link voltages in phases *b* and *c*, such

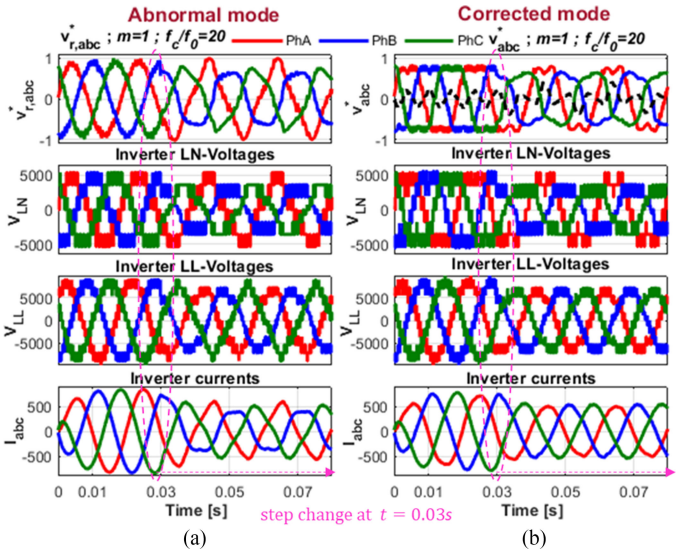

Fig. 18. Simulation results for a seven-level CHB inverter with dc-bus voltage step change in phases B and C at $t = 0.03$ s. $v_{\mathrm{dc},\,a} = [1\ \ 1\ \ 1]$; $v_{\mathrm{dc},\,b} = [0.3\ \ 1\ \ 0.7]$; $v_{\mathrm{dc},\,c} = [1\ \ 0.6\ \ 0.4]$, $m = 1$.

that $v_{\mathrm{dc},\,a} = [1\ 1\ 1]$; $v_{\mathrm{dc},\,b} = [0.3\ 1\ 0.7]$; $v_{\mathrm{dc},\,c} = [1\ 0.6\ 0.4]$. In Fig. 18(a) and (b), for $t < 0.03$ s, it can be observed that the inverter produces balanced output voltages and currents because there are equal dc voltages at the input dc links of all the bridges. When sudden step changes are simultaneously applied to dc-link voltages in phase *b* (cells *b*1 and *b*3) and in phase *c* (cells *c*2 and *c*3), the inverter operating without any correction method produces unbalanced voltages and currents, as shown in Fig. 18(a) for $t \geq 0.03$ s, whereas as shown in Fig. 18(b), the fluctuation of the dc-link voltage is corrected through online angle readjustment and both inverter output LL voltages and currents have been successfully rebalanced.

Case B: From the same normal operating condition, a sudden loss of one power cell is applied at $t = 0.03$ s on phase *a* such that: $v_{\mathrm{dc},\,a} = [0\ 1\ 1]$; $v_{\mathrm{dc},\,b} = [1\ 1\ 1]$; $v_{\mathrm{dc},\,c} = [1\ 1\ 1]$.

To correct this system, the tasks discussed in Section V must be executed during the transient. In this case study, the transient time is fixed at 50 ms (about 2.5 grid cycles). If the PWM reference voltages are not corrected within this transient time window, the system can resume its operation at $t = 0.08$ s (0.03 s + 0.05 s) and the inverter operation can continue by producing unbalanced voltages and currents, as shown in Fig. 19(a). However, Fig. 19(b) shows the balanced output LL voltages and currents when the proposed control strategy is applied within the transient time.

This confirms the effectiveness of the proposed compensation mechanism. It should be noted that during the 50 ms window when PWM signals are disabled, the inverter output voltage is identical to the grid voltage.

VII. Experimental Validations

Fig. 20 shows the 18-kW three-phase experimental laboratory test bench built to validate the effectiveness of the proposed control and modulation strategies. The experimental setup has

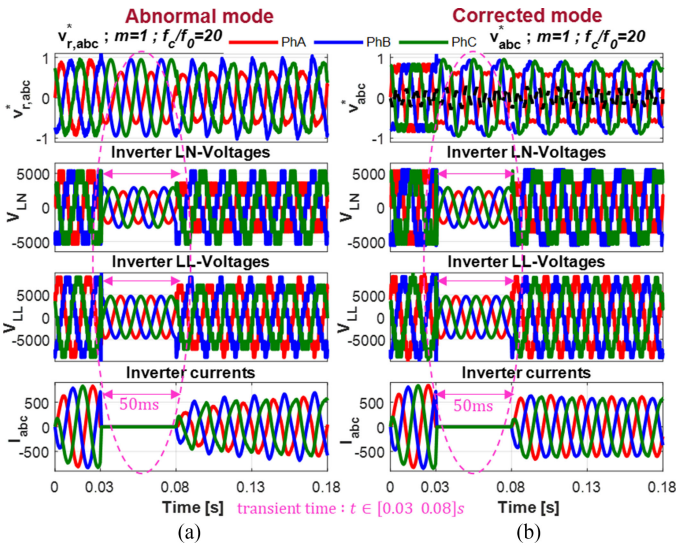

Fig. 19. Simulation results for a seven-level CHB inverter with a sudden loss of one power cell in phase A at $t = 0.03$ s. $v_{\mathrm{dc},\,a} = [0\ \ 1\ \ 1]$; $v_{\mathrm{dc},\,b} = [1\ \ 1\ 1]$; $v_{\mathrm{dc},\,c} = [1\ \ 1\ \ 1]$, $m = 1$.

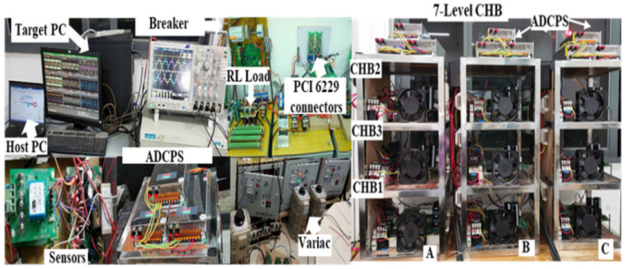

Fig. 20. Simulation and experimental hardware setup.

nine isolated H-bridges, which form a three-phase seven-level inverter in normal operation mode. Each H-bridge module is based on Semikron SK 10GD12T4ET and rated at 1200 V, 15 A. The changing meteorological conditions have been emulated by supplying each power module through an adjustable dc-power supply, model NES-1000-80 rated at 80 V, 12.5 A. This device operates as a variable current source feeding a dc power within a converter-specific voltage range to the dc input of the H-bride cell, which is used to emulate changes in meteorological conditions since it is possible to supply the H-bridge modules on a given phase with different dc-voltage values. The inverter three-phase legs are connected WYE, with a floating neutral point. The control hardware remains the same as the one used for the real-time simulation, which is connected to the hardware power stage through a data acquisition board NI-PCI 6229. The implemented sampling time for the control is 100 μs. To enable a power module bypass option, a contactor is added to the output of each H-bridge cell.

Protective functions #25 and #87 of the standard IEEE Standard C37.2-2008 have been developed to protect the experimental test bench and implemented to operate the output breaker. Function #25 prevents the output breaker to close in the case of a bad synchronization with laboratory grid, whereas function #87 prevents the output breaker to close if there is an unbalanced current and protects the system under test when a high differential current is present. To avoid unexpected shutdowns, the experimental test bench with a bypassed cell or partial dc-link voltage supply in some bridges has been not connected to the laboratory grid without correction. Consequently, an *RL*-load ($R = 15\ \Omega,$ and $L = 30$ mH) is used in all cases for allowing a proper analysis and comparison of the system behavior in both abnormal and corrected modes. A large resistance is selected to keep the converter within its current limits. The used inductance was the one available for tests, but a smaller value would have been preferred. However, the overall system behavior to be validated remains the same. The nominal dc-link voltage of each H-bridge dc-bus voltage used in the test is 50 V. All the individual dc-link source voltages ($v_{\mathrm{dc},\,ij}$) in a given phase leg are measured using dc-voltage sensors (model CHV-100/800). Each total leg dc-bus voltage $V_{\mathrm{dc},i}$ is then synthetized to be used in the angle calculation function as previously described in Section V. In every control cycle, the phase voltage angles for a given abnormal condition are computed within a quarter of the sampling time. The tested experimental conditions are given in Table I. A Tektronix oscilloscope MD04104C with voltage probes ET5001 and current probes TPP100 was used for mesurements. The experimental results were saved as text files, imported in a personal computer, plotted using MATLAB for increased clarity, and grouped in an organized way, as shown in Figs. 21 and 22.

TABLE I
TESTED ABNORMAL CONDITIONS

Cases	$v_{dc,a}$(V)	$v_{dc,b}$(V)	$v_{dc,c}$(V)
1)	[25 50 25]	[50 50 50]	[50 50 50]
2)	[50 50 50]	[50 0 50]	[30 20 40]
3)	[50 50 50]	[35 50 15]	[50 50 50]
4)	[0 40 10]	[50 50 50]	[50 50 50]

In *case 1*, it is assumed that changing meteorological conditions cause a voltage imbalance in the system by producing unequal dc-link voltages in phase *a*. In this case, the converter output currents and voltages are unbalanced, as shown in Fig. 21(a). However, both currents and LL voltages are successfully rebalanced by the proposed method, as shown in Fig. 21(b).

Similar experimental results are shown in Fig. 21(c) and (d) for *case 2*, which considers abnormal conditions in two phases. In phase *b*, one H-bridge module failure is considered, whereas in phase *c*, all the three PV-powered H-bridge modules are supplied with the partial dc-link voltage with the respect to their nominal value. Again, the proposed method is able to rebalance the currents and voltages.

In *case 3*, only PV mismatches are assumed, causing an unequal input power at inverter dc side (phase *b*) and unbalanced voltages and currents at the inverter ac side, as shown in Fig. 22(a). However, the neutral-shift strategy combined with the min–max zero-sequence injection is able to provide

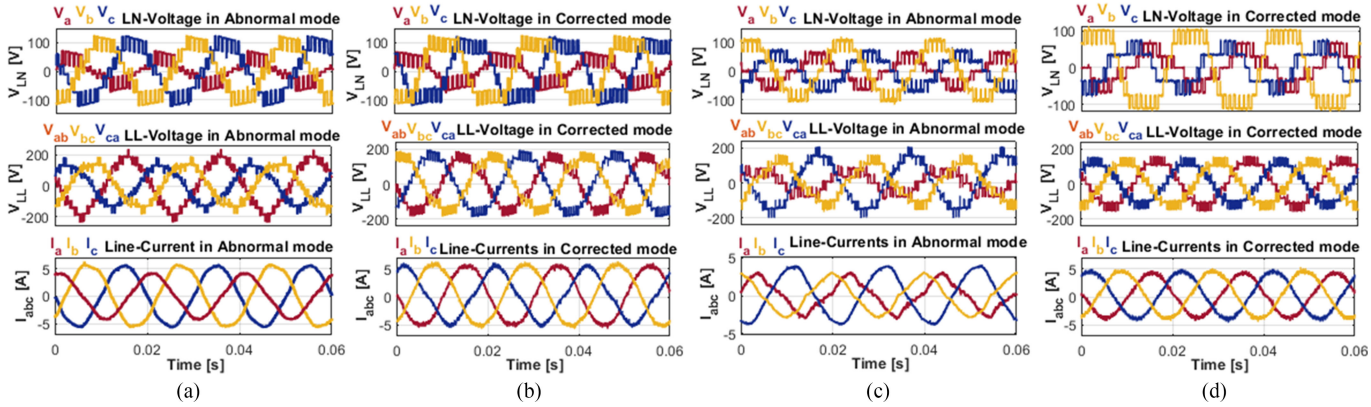

Fig. 21. Experimental results for a seven-level CHB inverter with $f_c/f_0 = 20$. (a), (b) Case 1: $v_{\mathrm{dc},\,a} = [25\ \ 50\ \ 25]$; $v_{\mathrm{dc},\,b} = [50\ \ 50\ \ 50]$; $v_{\mathrm{dc},\,c} = [50\ \ 50\ \ 50]$, $m = 1$. (c), (d) Case 2: $v_{\mathrm{dc},\,a} = [\,50\ \ 50\ \ 50\,]$; $v_{\mathrm{dc},\,b} = [50\ \ 0\ \ 50]$; $v_{\mathrm{dc},\,c} = [30\ \ 20\ \ 40]$, $m = 1$.

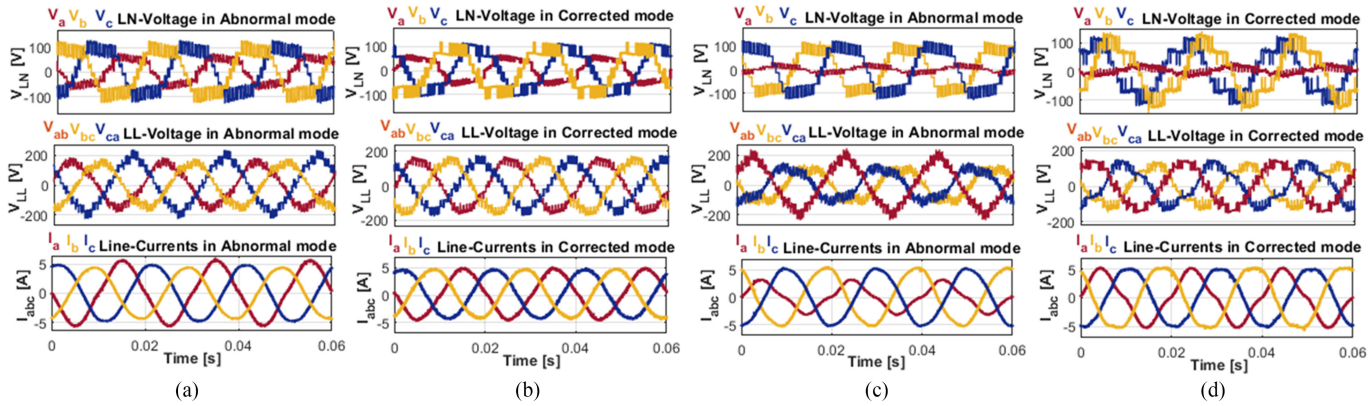

Fig. 22. Experimental results for a seven-level CHB inverter with $f_c/f_0 = 20$. (a), (b) Case 3: $v_{\mathrm{dc},a} = [50\ \ 50\ \ 50]$; $v_{\mathrm{dc},\,b} = [35\ \ 50\ \ 15]$; $v_{\mathrm{dc},\,c} = [50\ \ 50\ \ 50]$, $m = 1$. (c), (d) Case 4: $v_{\mathrm{dc},\,a} = [0\ \ 40\ \ 10]$; $v_{\mathrm{dc},\,b} = [50\ \ 50\ \ 50]$; $v_{\mathrm{dc},\,c} = [50\ \ 50\ \ 50]$, $m = 1$.

the three-phase balanced currents and voltages, as shown in Fig. 22(b).

In *case 4*, one H-bridge module of phase a (cell $a1$) has been bypassed and the remaining H-bridge power modules (cells $a2$ and $a3$) have been supplied with fractional dc-voltage values with respect to the nominal dc voltage $v_{\mathrm{dc,\,nom}} = 50$ V such that:$v_{\mathrm{dc},\,a1} = 0$, $v_{\mathrm{dc},\,a2} = 80\%\ v_{\mathrm{dc,\,nom}}$, and $v_{\mathrm{dc},\,a3} = 20\%\ v_{\mathrm{dc,\,nom}}$. This phase experiences a loss of 67% of its original voltage leading unbalanced output voltages and currents, as shown in Fig. 22(c), where no correction method has been applied. We can also observe in the same figure that the line current in phase a (i_a) is strongly distorted due the effect of saturation of the inductance caused by the high degree of imbalance. However, as shown in Fig. 22(d), in the corrected operation mode, both inverter output LL voltages and currents have been rebalanced, although the current in phase a (i_a) remains distorted as it is still influenced by the inductance saturation effect.

VIII. Conclusion

This article proposes a generalized neutral-shift modulation strategy combined with the minimum–maximum zero-sequence/homopolar injection to control PV cascaded multilevel inverter under changing meteorological conditions or with failed cells. The main challenge of the proposed control strategy is to produce both balanced inverter output LL voltages and currents under aforementioned abnormal conditions. The exploration is based on a time-domain evaluation supported by a space vector analysis of both inverter common-mode and differential-mode quantities, including their interactions. Graphical analysis, simulation and experimental results have been presented to show the effectiveness of this solution. The proposed control approach has a wide applicability in grid-tie applications, since it satisfies the requirements of functions #25 and #87 of IEEE Standard C37.2-2008. Thus, it allows a better utilization of PV sources connected to the grid and, at the same time, increases the robustness of the solution to failed converter modules.

It has to be pointed out that the developments presented in this article are focused on a large-scale PV energy collection application where several megawatts of solar power are transferred to the grid. It has been assumed that the converter is connected at the 3.3 kV bus of the distribution substation, even though a higher connecting point can be chosen depending on the overall power rating of the converter in order to reduce the IGBT current rating. It is also to be noted that this type of converter and the proposed analysis and control methods are also suitable for

standalone applications, such as medium-voltage motor drive systems.

REFERENCES

[1] K. Wang, R. Zhu, C. Wei, F. Liu, X. Wu, and M. Liserre, "Cascaded multilevel converter topology for large-scale photovoltaic system with balanced operation," *IEEE Trans. Ind. Electron.*, vol. 66, no. 10, pp. 7694–7705, Oct. 2019.

[2] A. Kumar and V. Verma, "Performance enhancement of single-phase grid-connected PV system under partial shading using cascaded multilevel converter," *IEEE Trans. Ind. Appl.*, vol. 54, no. 3, pp. 2665–2676, May/Jun. 2018.

[3] B. Xiao, L. Hang, J. Mei, C. Riley, L. M. Tolbert, and B. Ozpineci, "Modular cascaded H-bridge multilevel PV inverter with distributed MPPT for grid-connected applications," *IEEE Trans. Ind. Appl.*, vol. 51, no. 2, pp. 1722–1731, Mar. 2015.

[4] J. Chavarria, D. Biel, F. Guinjoan, C. Meza, and J. J. Negroni, "Energy-balance control of PV cascaded multilevel grid-connected inverters under level-shifted and phase-shifted PWMs," *IEEE Trans. Ind. Electron.*, vol. 60, no. 1, pp. 98–111, Jan. 2013.

[5] Y. Yu, G. Konstantinou, B. Hredzak, and V. G. Agelidis, "On extending the energy balancing limit of multilevel cascaded H-bridge converters for largescale photovoltaic farms," in *Proc. Australas. Univ. Power Eng. Conf.*, 2013, pp. 1–6.

[6] P. Sochor and H. Akagi, "Theoretical comparison in energy-balancing capability between star- and delta-configured modular multilevel cascade inverters for utility-scale photovoltaic systems," *IEEE Trans. Power Electron.*, vol. 31, no. 3, pp. 1980–1992, Mar. 2016.

[7] P. M. Lingom, J. Song-Manguelle, J. M. Nyobe-Yome, D. L. Mon-Nzongo, T. Jin, and M. L. Doumbia, "Control of a cascaded H-bride multilevel inverter with failed cells for grid-connected application," in *Proc. IEEE 10th Int. Symp. Power Electron. Distrib. Gener. Syst.*, 2019, pp. 806–811.

[8] S. Rivera, S. Kouro, B. Wu, J. Leon, J. Rodriguez, and L. Franquelo, "Cascaded H-bridge multilevel converter multistring topology for large scale photovoltaic system," in *Proc. IEEE Int. Symp. Ind. Electron.*, Jun. 2011, pp. 1837–1844.

[9] Y. Yu, G. Konstantinou, B. Hredzak, and V. G. Agelidis, "Power balance of cascaded H-bridge multilevel converters for large-scale photovoltaic integration," *IEEE Trans. Power Electron.*, vol. 31, no. 1, pp. 292–303, Jan. 2016.

[10] Y. Yu, G. Konstantinou, B. Hredzak, and V. G. Agelidis, "Power balance optimization of cascaded H-bridge multilevel converters for large-scale photovoltaic integration," *IEEE Trans. Power Electron.*, vol. 31, no. 2, pp. 1108–1120, Feb. 2016.

[11] Y. Yu, G. Konstantinou, B. Hredzak, and V. G. Agelidis, "Operation of cascaded H-bridge multilevel converters for large-scale photovoltaic power plants under bridge failures," *IEEE Trans. Ind. Electron.*, vol. 62, no. 11, pp. 7228–7236, Nov. 2015.

[12] Y. Yu, G. Konstantinou, C. D. Townsend, and V. G. Agelidis, "Comparison of zero-sequence injection methods in cascaded H-bridge multilevel converters for large-scale photovoltaic integration," *IET Renewable Power Gener.*, vol. 11, no. 5, pp. 603–613, May 2017.

[13] Electrical Power System Device Function Numbers, Acronyms, and Contact Designations, IEEE Standard C37.2-2008, Oct. 2008.

[14] P. W. Hammond, "Enhancing the reliability of modular medium-voltage drives," *IEEE Trans. Ind. Appl.*, vol. 49, no. 5, pp. 948–954, Oct. 2002.

[15] M. Aleenejad, H. Mahmoudi, and R. Ahmadi, "Unbalanced space vector modulation with fundamental phase shift compensation for faulty multilevel converters," *IEEE Trans. Power Electron.*, vol. 31, no. 10, pp. 7224–7233, Oct. 2016.

[16] F. Carnielutti, H. Pinheiro, and C. Rech, "Generalized carrier-based modulation strategy for cascaded multilevel converters operating under fault conditions," *IEEE Trans. Ind. Electron.*, vol. 59, no. 2, pp. 679–689, Feb. 2012.

[17] J. Lamb, B. Mirafzal, and F. Blaabjerg, "PWM common mode reference generation for maximizing the linear modulation region of CHB converters in islanded microgrids," *IEEE Trans. Ind. Electron.*, vol. 65, no. 7, pp. 5250–5259, Jul. 2018.

[18] D. G. Holmes and T. A. Lipo, *Pulse Width Modulation for Power Converters: Principles and Practice*. Piscataway, NJ, USA: IEEE Press, 2003.

[19] T. J. Summers, R. E. Betz, and G. Mirzaeva, "Phase leg voltage balancing of a cascaded H-bridge converter based STATCOM using zero sequence injection," in *Proc. Eur. Conf. Power Electron. Appl.*, 2009, pp. 1–10.

[20] M. Aleenejad, H. Mahmoudi, S. Jafarishiadeh, and R. Ahmadi, "Fault-tolerant space vector modulation for modular multilevel converters with bypassed faulty submodules," *IEEE Trans. Ind. Electron.*, vol. 66, no. 7, pp. 2463–2473, Mar. 2019.

[21] M. Veenstra, "Investigation and control of hybrid asymmetric multi-level inverter for medium-voltages applications," Thesis N°2843, Faculté des sciences et techniques de l'ingénieur, École Polytechnique Fédérale de Lausanne, Lausanne, Switzerland, 2003.

[22] M. Veenstra and A. Rufer, "PWM-control of multi-level voltage-source inverters," in *Proc. IEEE 31st Annu. Power Electron. Spec. Conf.*, Jun. 2000, vol. 3, pp. 1387–1393.

[23] J. Song-Manguelle, T. Thurnherr, S. Schröder, A. Rufer, and J.-M. Nyobe-Yome, "Re-generative asymmetrical multi-level converter for multi-megawatt variable speed drives," in *Proc. IEEE Energy Convers. Congr. Expo.*, 2010, pp. 3683–3690.

[24] J. Rodriguez, P. W. Hammond, J. Pontt, R. Musalem, P. Lezana, and M. J. Escobar, "Operation of a medium-voltage drive under faulty conditions," *IEEE Trans. Ind. Electron.*, vol. 52, no. 4, pp. 1080–1085, Aug. 2005.

[25] J. Han, X. Kong, P. Li, Z. Zhang, and X. Yin, "A novel low voltage ride through strategy for cascaded power electronic transformer," *Protection Control Modern Power Syst.*, vol. 4, no. 3, pp. 227–238. Oct. 2019.

[26] B. Bahrani, S. Kenzelmann, and A. Rufer, "Multivariable-PI-based DQ current control of voltage source converters with superior axis decoupling capability," *IEEE Trans. Ind. Electron.*, vol. 58, no. 7, pp. 3016–3026, Jul. 2011.

[27] "SINAMICS Perfect Harmony GH180: Medium voltage air-cooled drives," Catalogue D.15.3, Jun. 2017. [Online]. Available: https://cache.industry.siemens.com/dl/files/601/109749601/att_927522/v1/SINAMICS_GH180_OperatingInstructions_EN_AirCooled_6SR41.pdf

P. M. Lingom (Student Member, IEEE) was born in Edea, Cameroon, in 1994. He received the B.S. and M.S. degrees in pedagogical sciences and electrical engineering from the University of Douala, Douala, Cameroon, in 2014 and 2016, respectively. He is currently working toward the Ph.D. degree with the Department of Electrical Engineering and Automation, Fuzhou University, Fuzhou, China.

His research interests include analysis and control of multilevel power converters, as well as control of renewable energy systems.

Joseph Song-Manguelle (Senior Member, IEEE) received the B.S. and M.S. degrees in pedagogical sciences and electrical engineering from the University of Douala, Douala, Cameroon, in 1995 and 1997, respectively, and the Ph.D. degree in electrical engineering from the Swiss Federal Institute of Technology, Lausanne, Switzerland, in 2004.

From 2004 to 2012, he held engineering positions with General Electric in Germany, France, and USA, where he was involved in the development of torsional vibration control systems with VFDs and HVDC transmission and distribution systems for future long tieback subsea applications. Since 2012, he has been with an oil and gas corporation, where he has held several engineering positions in Texas, Russia, and Papua New Guinea. His activities are ranging from technical qualification of subsea electrical components to electrical design, modification, and troubleshooting of oil and gas production facilities. In parallel to his professional industrial activities, since 2010, he has been cosupervising master's and Ph.D. students at the University of Douala, Fuzhou University, Fuzhou, China, and the Université du Québec à Trois-Rivières, Trois-Rivières, QC, Canada, where is an Adjunct Professor. He also holds four patents. His university research activities include theoretical understanding of VFDs' harmonics and their interaction with large rotating shafts, as well as control of renewable energy systems.

Dr. Song-Manguelle is a member of the IEEE Petroleum and Chemical Industry and the Industrial Drives and the Power Electronics Committees. He is an Associate Editor for the IEEE TRANSACTIONS ON INDUSTRY APPLICATIONS.

Daniel Legrand Mon-Nzongo (Member, IEEE) was born in Douala, Cameroon, in 1986. He received the B.S. and M.S. degrees from Douala University, Douala, Cameroon, in 2010 and 2012, respectively, and the Ph.D. degree from Fuzhou University, Fuzhou, China, in 2018, all in electrical engineering.

Since June 2018, he has been a Postdoctoral Research Associate with Fuzhou University and Pearl Electric Co., Ltd., Guangzhou, China. His research interests include bidirectional multilevel ac/ac and isolated dc/dc converters for medium-voltage applications.

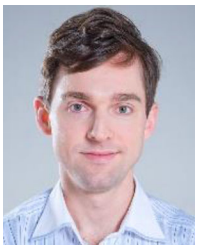

Rodolfo César Costa Flesch (Member, IEEE) received the B.E., M.Eng., and Dr.Eng. degrees in control and automation engineering from the Federal University of Santa Catarina (UFSC), Florianópolis, Brazil, in 2006, 2009, and 2012, respectively.

He is currently a Professor with the Department of Automation and Systems Engineering, UFSC, and a Researcher with the Brazilian National Council for Scientific and Technological Development, Brasília, Brazil. In addition, he is the co-ordinator of several R&D cooperation projects between academy and industry. His research interests include process control (time-delay processes and model predictive control), instrumentation, and automation of tests.

Tao Jin (Senior Member, IEEE) received the B.S. and M.S. degrees from Yanshan University, Qinhuangdao, China, in 1998 and 2001, respectively, and the Ph.D. degree from Shanghai Jiao Tong University, Shanghai, China, in 2005, all in electrical engineering.

From 2005 to 2007, he was a Postdoctor with Shanghai Jiao Tong University, and was also in charge of a research group in the biggest dry-type transformer company in Asia, Sunten Electrical Co., Ltd, to develop new transformer technology with distribution grid. From 2008 to 2009, he was a Research Scientist with Virginia Tech, Blacksburg, VA, USA, where he was involved in the design and test of PMU technology and GPS/internet-based power system frequency monitoring network. In 2010, he joined as a European Union Marie Curie Research Fellow with the Imperial College London, London, U.K., where he was focused on electrical technologies related to smart grid. He is currently a Professor with the College of Electrical Engineering and Automation, Fuzhou University, Fuzhou, China. He has authored/coauthored about 150 papers.

Prof. Jin is currently an Associate Editor for *Journal of Modern Power Systems and Clean Energy*, *Protection and Control of Modern Power Systems*, *China Measurement and Testing Technology*, and several other journals. He is a member of the IEEE Power and Energy Society and IEEE Industrial Electronics Society, and Special Committee Member of the Chinese Society of Electrical Engineering, China Electrotechnical Society, etc.